Published in final edited form as:
Nat Nanotechnol. 2009 January ; 4(1): 56–63. doi:10.1038/nnano.2008.360.

Tuning the Optical and Electronic Properties of Colloidal Nanocrystals by Lattice Strain

Andrew M. Smith, **Aaron M. Mohs**, and **Shuming Nie***
Departments of Biomedical Engineering and Chemistry, Emory University and Georgia Institute of Technology, 101 Woodruff Circle, Suite 2001, Atlanta, Georgia 30322, USA

Abstract

Lattice strain is a structural parameter that has been exploited in microelectronic devices with great success, but its role in colloidal nanocrystals is still poorly understood. Here we have developed strain-tunable colloidal nanocrystals by using lattice-mismatched heterostructures that are grown by epitaxial deposition of a compressive shell (e.g., ZnSe or CdS) onto a soft and small nanocrystalline core (e.g., CdTe). This combination of a “squeezed” core and a “stretched” shell causes dramatic changes in both the conduction and valence band energies. As a result, we show that core-shell QDs with standard type-I behavior are converted into type-II nanostructures, leading to spatial separation of electrons and holes, extended excited state lifetimes, and giant spectral shifting. This new class of strain-tunable QDs exhibits narrow light emission with high quantum yield across a broad range of visible and near-infrared wavelengths (500 nm to 1050 nm).

Introduction

The impact of strain on materials is fundamentally important to a broad range of fields, from optoelectronics to biomechanics. Recent studies have explored the complex relationship between nanomaterials and strain, demonstrating that nanostructures with novel properties can be generated through lattice strain,[1,2] and that nanomaterials respond differently to strain compared to their bulk counterparts.[3–5] Semiconductor quantum dots (QDs), typically prepared as (core)shell nanocrystals, are a class of strained materials of considerable current interest because of their novel optical and electronic properties. The fluorescence efficiency of these materials is believed to be detrimentally affected by the lattice mismatch between the core and shell materials,[6–9] but other effects of epitaxial strain have been largely unexplored. In crystalline solids, stress-induced changes in the lattice parameters alter the intrinsic inter-atomic distances, and modify the energy levels of bonding electrons. In a crystalline semiconductor, this deformation significantly changes its electronic and optical properties such as the absorption and emission band edges.[10–12] This effect has been under intense study in optoelectronics, as materials strain is inherent in the epitaxial growth of lattice-mismatched heterostructures, and has been used to develop lasers and light emitting diodes consisting of semiconductor films that are strained by their growth substrates.[13,14] By straining thin layers within the quantum confinement regime, the interplay between quantum confinement and lattice strain can yield a high level of control in bandgap engineering. This control may be broadened by replacing the quantum wells with zero-dimensional quantum dots, which are more strongly confined, and may be spontaneously deposited on a lattice-mismatched substrate in the Stranski-Krastanov growth mode.[13] These self-assembled QDs can be prepared with reproducible and controllable sizes and uniform patterns. However, their fabrication costs are

*Corresponding author, email: E-mail: snie@emory.edu.

Competing financial interests. The authors declare no competing financial interests.

high, and these QDs are island-like, rarely forming zero-dimensional spherical morphologies. In contrast, colloidal syntheses of QDs have demonstrated an exquisite degree of control over both size and shape, with excellent monodispersity, high quantum yields (approaching unity), and much lower costs. Because of these advantages, recent work has started to integrate these particle suspensions into solid-phase devices.[15,16]

Compared to bulk epitaxy, strain is expected to manifest itself uniquely in colloids due to the ability of an epitaxial layer to strain its substrate. This "double straining" effect changes the properties of both the epitaxial layer and the substrate. In fact, our experimental data and elasticity calculations demonstrate that a very high level of strain can be tolerated in small nanocrystals, compared to what is achievable in bulk materials. Small nanocrystals (<5 nm) have a high surface area-to-volume ratio and highly curved surfaces, allowing the stress from a lattice-mismatched epitaxial shell to be distributed over a large fraction of the constituent atoms. For larger nanocrystals and bulk substrates, the total number of atoms is larger, and the epitaxial stress is imposed on a surface that contains a smaller fraction of the constituent atoms, favoring the formation of strain-relaxing crystalline defects rather than homogenous strain.

In this work, we report that heteroepitaxial strain within core/shell QDs can be used to dramatically impact the optical properties of these nanocrystals. In particular, the epitaxial growth of a compressive shell material (ZnS, ZnSe, ZnTe, CdS, or CdSe) on a small and soft nanocrystalline core (CdTe) leads to a large change in the conduction energy band of the resulting heterostructures. We show that lattice strain can be used to control the locations of charge carriers, to modulate the excited state lifetimes, and to tune the absorption and emission spectra across a wide wavelength range. These results are dramatically different the small red shifts in the emission spectra (5–7 nm) observed by Chen et al. for CdSe QDs during the growth of a CdS shell. Their reported synthesis conditions are known to be incompatible with heteroepitaxial shell growth of CdS, and the observed small spectral shifts are most likely not caused by lattice strain, but arise instead from the growth of CdSe cores (not CdS shells) under their experimental conditions.

Results and Discussion

Strain Tuning in Colloidal Nanocrystals

As illustrated in Figure 1, lattice strain can induce significant bandgap energy changes when a shell material is coherently grown on a small and compressible nanocrystalline core. In the bulk state, heterostructures of CdTe and ZnSe have valence and conduction bands that are aligned to localize both the electrons and holes in CdTe (type-I behavior). On the nanometer scale, however, epitaxial growth of a ZnSe shell strongly compresses a CdTe nanocrystal because the lattice parameter of ZnSe (5.668 Å) is considerably smaller than that of CdTe (6.482 Å). For nearly all zinc-blende II-VI and III-V semiconductors, the electronic energy gap increases with applied compressive force, and decreases under tensile strain, an effect that has been experimentally observed and theoretically predicted.[10,17] This is represented by a negative deformation potential (a<0), defined as

$$a = \frac{\partial E_{g,o}}{\partial(\ln V)}$$

where $E_{g,o}$ is the bandgap of the unstrained semiconductor and $\partial(\ln V)$ is the fractional volume change. The conduction band shifts to a much larger degree than the valence band,[18] and therefore the compressive deformation of CdTe (a_{ZnSe} = −3.70 eV) induced by shell growth increases the energy of the conduction band. At the same time, the shell material (a_{ZnSe} = −4.99 eV) is under tensile strain, resulting in a decrease in its conduction band energy. These two

strain effects work in a concerted fashion (that is, double straining) to alter the energy band offsets, converting standard type-I QDs into type-II heterostructures, resulting in a spatial separation of the electrons and holes. As the shell grows in thickness, the core conduction band energy rises due to increased compressive strain from the shell, while the shell's conduction band energy decreases due to a reduction in quantum confinement.

Properties of Strain-Tuned Nanocrystals

With increasing epitaxial shell growth of ZnSe on CdTe, the optical absorption and fluorescence emission spectra are dramatically shifted toward longer wavelengths (lower energies) (Figure 2A). Small spectral changes are also observed in type-I QDs when a finite potential well of the shell allows tunneling of the electron and hole between the core and the shell.[6,19] In the case of (CdTe)ZnSe, however, additional shell growth continues to shift the absorption band-edge and the emission maximum, beyond the band-edge energy of bulk CdTe (1.50 eV) and ZnSe (2.82 eV) (see Figure 2A and 2B). Several lines of evidence suggest that this red shift is due to a transformation to type-II band alignment for these (core)shell QDs: (i) a gradual reduction of distinct optical absorption features; (ii) a decrease in the band-edge oscillator strength, and (iii) a significant increase in excited state lifetimes (Figure 2D). These changes are caused by spatial separation of holes into the core and electrons into the shell, resulting in a decrease in the electron-hole overlap integral. As reported by Kim et al., colloidal type-II quantum dots such as (CdTe)CdSe, can achieve charge carrier separation through the selection of specific materials with staggered band offsets for the core and shell.[20] Energy band offset and electron-hole separation allow spatially indirect recombination at energies lower than the bulk bandgap energies of either of the individual semiconductors.

The largest spectral shifts are observed with very small cores, such as 1.8 nm CdTe, allowing tuning from the green to the near-infrared spectra. In contrast, larger CdTe cores cannot be effectively compressed through epitaxy, and their emission spectra are much less tunable by lattice strain. The strain-tunable spectral ranges are shown in Figure 2C for different sized CdTe cores. It is remarkable that QDs with small cores can be tuned to emit beyond the spectral ranges of large dots, at both ends of the emission spectra. This novel phenomenon has not been observed for other types of quantum dots and cannot be explained by conventional factors (for a more detailed explanation, see Supplementary Discussion). Depending on the core size and shell thickness, these QDs can be tuned to emit between 500 nm and 1050 nm with a quantum efficiency between 25–60%. The fluorescence peak width is consistently between 40 and 90 nm (full-width-at-half-maximum or FWHM) in the near infrared (700 – 900 nm), a "clear window" well suited for biomedical imaging applications.

An interesting finding is that the strain-induced spectral changes are gradual and do not exhibit abrupt transformations as might be expected for a switch from type-I to type-II. For core sizes less than 4 nm diameter, our data indicate that the transition to type-II behavior is "complete" after capping with 2–3 monolayers (ML) of shell material. Between 0 and 2–3 ML, however, the behavior of these QDs is between type I and type II, a regime that has been dubbed 'quasi-type-II' in the literature.[21] Here one of the charge carriers is strongly confined to one region of the nanocrystal (in our case, the hole is confined to the core), whereas the other charge carrier (the electron) is only weakly confined, being largely delocalized across the entire nanocrystal. See Supplementary Figure 1 for further information about this gradual transition.

Strain Tuning in Multilayered Structures

To further understand the separation of electrons and holes in these strained nanostructures, we have carried out systematic capping experiments in which interim shell layers are used to provide specific energy barriers to either the hole or the electron (Figure 3). Capping CdTe with a CdSe shell is known to generate type-II QDs with the electron located in the shell, due

to the lower conduction band energy level of CdSe compared to CdTe. In contrast, capping CdTe with a ZnTe shell or an interim layer of ZnTe provides a large barrier to electron diffusion out of the QD core, but little impediment to hole diffusion out of the core. As expected, capping CdTe with CdSe yields a type-II QD with a substantial decrease of the band gap, whereas ZnTe capping only slightly changes the band gap. By using one monolayer of these materials as a barrier to hole or electron diffusion, overgrowth of ZnSe leads to a type-II structure only when grown with the CdSe interim layer. Very little red-shift is observed for QDs with an interim layer of ZnTe, confirming that electron diffusion into the shell is essential for the strain-induced type-II structure to function. Hole confinement to the core is also supported by the high quantum efficiency of these core/shell QDs, as surface hole traps are more detrimental to the optical properties of QDs than are electron traps.[20,22–24]

It is remarkable that the highly strained (CdTe)ZnSe heterostructures (14.4% lattice mismatch) are able to maintain excellent photoluminescence properties. We attribute the high quantum yield to the high crystallinity of the initial CdTe cores (quantum yield up to 80%), and the homogeneity of shell growth at high temperatures (shell growth was incomplete and nonuniform below 200°C). Also, the lattice compressibility is considerably higher for CdTe (bulk modulus B_u = 42.4 GPa) and ZnSe (B_u = 62.4 GPa) (considered to be softer because of their lower modulus values) as compared to the commonly used QD materials of CdSe (B_u = 53.1 GPa) and ZnS (B_u = 77.1 GPa).[25] Thus, the ability of CdTe and ZnSe to elastically compress when subjected to a large stress, rather than relaxing to form defect trap sites, allows these QDs to maintain their excellent spectral properties. These QDs maintain a high quantum yield after 2 ML of shell growth (Figure 3B), unlike similarly strained (CdSe)ZnS QDs (12% lattice mismatch), which reach a peak in quantum yield after roughly 1.5 ML of shell growth. This difference is likely due to the inability of the less elastic CdSe and ZnS to withstand strain without forming defects. Using the softer CdTe core, we have succeeded in growing both CdS and ZnS shells (11.4% and 19.8% lattice mismatches, respectively), in which a high quantum yield is maintained even after 3 ML of shell growth (see Supplementary Figure 2 and Figure 3).

The concept of strain-induced defect formation has been the predominant paradigm for understanding the photoluminescence efficiency of (core)shell QDs,[6] but this concept does not account for the unexpectedly low quantum efficiencies of type-II QDs.[20] Xie et al. reported that type-II (ZnTe)CdSe QDs have a quantum yield of 15–20%, which decreases after growth of 1.5 ML, despite a lattice mismatch of only 0.6%.[26] In our own work, Figure 3B shows that type-II (CdTe)CdSe QDs (7.1% lattice mismatch) reach a peak in fluorescence efficiency after only 1 ML of shell growth, whereas highly strained (CdTe)ZnS QDs (~20% lattice mismatch) reach a peak fluorescence efficiency after 2.5–3 ML of shell growth (Supplementary Figure 3). The separation of charge carriers in type-II QDs can result in a decreased probability of radiative recombination, and the extended excited state lifetimes may increase the probability of nonradiative recombination events. In addition, one of the charge carriers in type-II QDs is confined to the shell region, and this carrier thus has an increased probability of being trapped in a surface defect site, a major factor governing the photoluminescence efficiency of QDs.

Direct Structural Characterization

Powder X-ray diffraction (XRD) data (Figure 4A) show that these QDs grow homogeneously as single crystalline domains. The CdTe cores show a zinc-blende crystal structure, which shifts to smaller bond lengths with shell growth, and the lattice becomes hexagonal. After 6 monolayers of shell growth, the lattice constant has shrunk by 5.1% relative to zinc-blende CdTe, indicating an expansion of the ZnSe shell lattice by 8.5% compared to bulk. Further increasing the shell thickness to 9 ML nearly doubles the total nanocrystal volume, but only slightly changes the lattice parameters. The diffraction peaks become narrower due to the larger

crystalline domains produced, with no evidence of pure ZnSe or CdTe domains or major defects. Combined with the quasi-spherical morphology of these particles observed in TEMs (Figure 4B), this data suggests that growth is crystalline, epitaxially coherent, and homogeneous, despite the large strain between these materials. As previously mentioned, defect formation is often correlated with a reduced radiative recombination efficiency, but these QDs maintain a high quantum yield throughout the shell growth, and only band-edge emission is observed even after 9 monolayers of ZnSe shell growth as shown in Supplementary Figure 4. The phase transition from zinc blende to wurtzite was not an expected observation, however there is only a small difference in energy between these two crystal structures, and CdTe has a propensity to transform to the softer wurtzite phase when subjected to epitaxial stress.[27] High-resolution TEM images verified this phase transition, which was also observed for several other core/shell QD structures (CdTe/CdS, CdSe/ZnS, CdTe/ZnTe, and CdTe/CdSe). Under the same experimental conditions, we found that small zinc-blend CdSe nanocrystals (~2 nm) also transition to the wurtzite phase after growth of ~6 monolayers of a ZnSe shell.

High-resolution TEM data (Figure 4C and 4D) reveal the coherent crystallinity of these QDs, with lattice planes extending throughout the entire nanocrystal. Besides sporadic multiple twinning (see Suppl Figure 7), no major crystalline defects are observed. Nearly all QDs (>95%) with shells larger than 2 monolayers are identified to be oriented with the wurtzite (001) plane parallel to the TEM grid. This anisotropy is in agreement with XRD patterns of samples with thick shells (Figure 4A) that show more intense and narrower diffraction peaks for the (110) plane compared to (112), as well as for (100) compared to (101). We attribute this preferential growth to the slightly larger lattice mismatch between these materials in the *a*-direction compared to the *c*-direction, and due to the higher compressibility of wurtzite II-VI materials in the [100] and [010] directions compared to the [001] direction.[25] As well, the zinc-blende core CdTe QDs are found to be slightly elongated in the [111] direction (Figure 4C), with an aspect ratio of ~1.4. Upon phase transition to wurtzite, this elongated direction becomes the [001] direction, suggesting that shell growth predominantly propagates in the radial direction outward along the cylindrically shaped QDs. This mode of shell growth contrasts with that observed for most CdSe nanocrystals, which typically favor growth in the [001] direction, commonly attributed to the high reactivity of the (001) facet and closer lattice match in this direction.[8,28,29] We have also observed lattice warping and electron-density differences, as might be expected from core-shell type structures (Supplementary Figure 8).

In terms of lattice compressibility and deformation potential, CdTe is the most compressible of all the II-VI and III-V materials except for mercury telluride, and its deformation potential is relatively high.[18] This means that the lattice of CdTe is readily compressed, and upon compression, its electronic energy bands shift to a large degree. ZnSe also has a high deformation potential but has a much higher bulk modulus; its role as a less deformable, highly mismatched shell material is likely crucial in generating the unique optical properties reported. In comparison, core-shell QDs with better lattice matching (such as (CdTe)CdS and (CdSe) CdS) exhibit considerably less spectral shifting due to the reduced lattice strain and lower deformation potential values. Furthermore, nearly all (core)shell nanocrystals and other types of nano-heterostructures are subject to varying degrees of lattice strain, because of structural mismatches between two different materials.

Continuum Elasticity Modeling

To gain further insights into the mechanism of strain tuning, we have implemented a continuum elasticity model for coherently grown epitaxial ZnSe shells on CdTe cores (Figure 5). With radial compression from the shell, the core is found to be under isotropic, compressive strain. The shell lattice is under tensile strain in the tangential directions surrounding the core, and compressively strained in the radial direction. The strain in the shell decays with increasing

distance from the interface, but does not decay fully to zero, in agreement with XRD data (Figure 4A) demonstrating the inability of thick shells to compress the core to more than a critical value, leaving a significant amount of elastic strain in the shell. This effect is also predicted to occur for even thicker shells (data not shown). When compared with the lattice constants experimentally observed from XRD and TEM, the compression of the core is calculated to be significantly larger. There are several factors underlying this discrepancy. Most importantly, this is due to the nonspherical growth in the shell, occurring mostly perpendicular to the c-axis, causing the heterostructure to more closely resemble concentric cylinders rather than concentric spheres. As shown in Figure 5A, modeling this system as cylinders redistributes much of the strain to the shell, and more strongly correlates with the experimentally observed lattice parameters. Using this theoretically derived lattice deformation we have used the model-solid theory to calculate the band offsets and bandgaps of the various (core)shell structures reported in this work. As shown in Supplementary Figure 9, we are also able to predict the bandgaps of these structures at various stages of shell epitaxial growth.

As the shell grows on the core, the strain energy within the nanocrystal may exceed the energy required to form a lattice defect, favoring strain relaxation. After calculating the energy of a dislocation loop at the (core)shell interface, total energy minimization reveals that CdTe QDs up to ~3.4 nm diameter can tolerate the strain imposed by any shell thickness of ZnSe without loss in structural coherency. This agrees with the experimental observation that larger cores are less strain-tunable, suggesting that this dependence is due to strain relaxation through dislocations. The main disagreement between the experimental data and the theoretical strain calculations is the prediction of abrupt changes in lattice constants at the core/shell interface, and the differences in radial and tangential lattice parameters in the shell. HRTEM data indicate that the entire QD is a coherent crystal, with little lattice deformation. Few literature observations have noted coherent lattice distortions in nanocrystals this small, which may be energetically unfavorable and reveal an inherent inaccuracy in the application of continuum elasticity models to very small nanoparticles. However, more complex atomistic models tend to agree strongly with continuum elasticity models, but smooth out rapid changes in strain.

For these modeling calculations, bulk materials parameters are used because no general trends have emerged regarding the dependence of materials properties on particle size. For some materials, their compressibilities change with grain size, most commonly showing a softening effect with decreasing size.[30–32] In other instances, however, their compressibility values are found to be unchanged in nanoparticles compared to the bulk.[30–32] For II-VI semiconductors, it has been reported that CdS QDs have similar compressibilities compared to the bulk,[30] whereas CdSe QDs are more compressible than the bulk material.[32] Quantum confinement by itself may induce structural modifications in semiconductor nanocrystals,[33] and these nanocrystals may be subject to compressive or tensile forces depending on the nature of their passivating ligands.[34] For the strain-tunable QDs in this work, the elasticities of nanoscale ZnSe and CdTe have not been determined as a function of particle size. If the elasticities of the core and shell materials decreased evenly, the total elastic strain energy in these dots would be reduced. This energy reduction is not expected to alter crystalline deformation or leads to major net changes in our bandgap calculations. To further examine the case in which only one of the materials becomes more elastic, we have implemented a theoretical model using smaller elastic moduli (example.g., 20% smaller than bulk) for either the core or shell materials. We find that this softening effect marginally modifies the magnitude of the strain-induced band shifting (by less than 3%). We also note that the observed phase transition during shell growth may slightly factor in the level of accuracy of the calculated bandgaps. Wei *et al.* calculated a bandgap 1.50 eV for zinc blende CdTe and a bandgap of 1.547 eV for wurtzite.[27] For ZnSe, experimental data of the bandgaps also reveal a very small difference of 2.82 eV for zinc blende,and 2.8474 eV for wurtzite.[35]

In conclusion, we have reported a new class of core-shell quantum dots (QDs) that are converted into type-II nanostructures by lattice strain. The strain-tunable QDs show narrow light emission with high quantum yields (60%) across a broad spectrum of visible and near-infrared wavelengths (500 nm to 1050 nm). The results provide key insights to the optical and electronic properties of CdSe/ZnS, CdSe/CdS, and other quantum nanostructures. In particular, the strain-induced type-II behavior leads to a spatial separation of electrons and holes, and prolonged excited state lifetimes, parameters that will be important to multi-exciton generation and efficient solar energy conversion.[21,36,37] Due to their near-infrared emission spectra and low cadmium content (one the CdTe core contains cadmium), this new class of compact QDs might be suitable for in-vivo animal imaging. We also envision that other colloidal semiconductor nanocrystals with similar bulk materials parameters could be employed for strain tuning, especially III-V antimonides (AlSb, GaSb, and InSb) and other II-VI tellurides (ZnTe and HgTe).

Methods

Synthesis of quantum dot cores

(Core)shell QDs were prepared by using a two-step organometallic approach in a high-temperature coordinating solvent.[7,38,39] CdTe cores of various sizes (1.8 – 6.2 nm) were synthesized by swiftly injecting a room-temperature solution of trioctylphosphine-telluride (0.1 mmol in 5 mL octadecene) into a hot (300°C) solution of cadmium oxide (0.2 mmol), tetradecylphosphonic acid (0.44 mmol), hexadecylamine (5.7 mmol), and octadecene (10 mL total). The growth temperature was set to 265°C and the final size of the CdTe QD core was controlled by varying the growth time, and by slow injection of additional precursors if larger sizes were desired. After cooling to room temperature, the highly luminescent nanoparticles (quantum efficiency 40–80%) were diluted in hexane, centrifuged to remove the insoluble cadmium precursor, purified via repeated hexane-methanol extractions, and finally centrifuged again to remove potential nanocrystal aggregates.

Detailed procedures for shell growth

Hexane solutions of purified quantum dots were diluted in oleylamine to roughly half of the concentration of their original reaction solution, typically in 10 mL reaction volumes. The reaction vessel was then attached to a Schlenk line, and degassed at room temperature to remove hexane. The solution was then refluxed under vacuum (~20 Pa) at ~100°C for an additional 40–60 minutes to ensure complete removal of oxygen, water, hexane, and other low boiling point impurities. The solution was then purged three times with argon, and the temperature of the solution was increased to the initial capping temperature (T_{ML1}). This temperature was empirically optimized to be as high as possible, to maximize the reactivity of the shell precursors, but low enough to inhibit the competing process of Ostwald ripening. The onset of Ostwald ripening was determined by heating QDs in oleylamine to 100°C for 10 minutes, measuring the absorption and emission spectra of the QDs to look for possible signs of ripening, and then ramping the temperature in 10°C increments and repeating this process. Note that these temperatures are significantly lower than those typically used for shell growth on CdSe cores, mainly due to the greater ripening propensity of CdTe compared to CdSe. A summary of the important experimental parameters is provided in Supplementary Table 2.

For the addition of shell precursors, we used a modified version of the successive ion layer adsorption and reaction (SILAR) procedure, originally described by Peng and coworkers.[39] Specifically, at the initial capping temperature, we injected a solution containing cation precursor (0.1 M diethylzinc or dimethylcadmium dissolved in TOP), containing the amount of precursor required to constitute a 0.25 ML shell. After 10 minutes, which we experimentally determined was a sufficient amount of time to prevent homogenous nucleation of the shell

material, we injected the anion precursor (0.1 M sulfur, selenium, or tellurium, dissolved in TOP). After this second injection, shell growth was allowed to proceed for a period of time dependent on the initial growth temperature and the shell composition. For example, for the growth of ZnSe on CdTe, the following reaction times were used: 4 hours for 150°C, 2 hour for 170°C, and 30 minutes for 210–225°C. For different shell materials, however, it was found that the shell growth rate was strongly dependent on the reactivity of the precursors. Both diethylzinc and dimethylcadmium were highly reactive at all of the temperatures used in this work, as we found that these reactions were limited by the deposition rate of the chalcogenide. Generally, tellurium and selenium reacted efficiently at low temperatures (e.g. 2 hours reaction time at 170°C), but initial growth of CdS and ZnS required extended times, up to 8 hours before completion on 2.0 nm cores at 150°C. After the first two injections at T_{ML1}, a second pair of injections was performed to grow 1 ML of total shell on the cores, using the same reaction time for the first 0.5 ML.

Once this thin layer of shell material was deposited on the QDs, indicated by spectral red-shifting, the temperature threshold of these QDs toward ripening was significantly enhanced. This is due to a combination of the increase in overall size of the nanocrystals, the greater bond strength and thermal stability of the shell materials used in this study (CdS, CdSe, ZnSe, ZnS, ZnTe) compared to the cores (CdTe), as well as the greater strength of bonding of the amine and phosphine ligands to the shell material, compared to CdTe. Thereby, after the deposition of just 1 ML, the temperature of the reaction could be increased drastically without optical signs of ripening. In this manner, the growth temperature was increased to a point at which the shell reaction was much more efficient, and shorter reaction times could be used to complete shell growth. The deposition of ZnSe on CdTe was optimized for all of the sizes tested, however the deposition of the other shell materials (ZnS, ZnTe, CdS, CdSe) was only optimized for 3.8 nm QD cores, although the extrapolation of this technique to other core sizes should like be straightforward by employing the methodology described herein. For this procedure, we chose to use 0.25 monolayer increments so that the surface stoichiometry of anions and cations would be similar for each 0.5 ML shell growth cycle. When performed with 0.5 ML increments, like the SILAR procedure originally described by Peng et al., there was a significant decrease in QY after each anion injection, thus obscuring the relative changes in fluorescence QY, which is in accord with previous findings.[39,40]

We tested a variety of alternative shell precursors for this work. We found that carboxylate salts of cadmium and zinc required a much higher reaction temperature compared to their organometallic counterparts. With fatty acid salts of zinc and cadmium, we were unsuccessful in capping the smallest CdTe cores without suffering from significant Ostwald ripening at the high temperatures required for efficient shell deposition. However larger cores (>4 nm) could be efficiently capped with these precursors. We also tested several chalcogenide precursors, including commonly used organosilicon compounds (e.g. hexamethyldisilathiane) and elemental chalcogenides in the absence of phosphines. These reagents were generally too reactive to prevent homogeneous nucleation of shell materials. Phosphine-chalcogenide precursors, however, were found to yield an excellent balance of resistance to nucleation and a high reactivity toward epitaxial growth.

Calculation of shell thickness

For our calculations of shell material additions, we employed an approach similar to that which is used in epitaxial overgrowth of thin films on bulk substrates. Specifically, with the deposition of a thin epilayer on a QD core, we make the assumption that the material deposits layer-by-layer as a coherent, epitaxial structure. Thereby, the core serves as a ‘substrate’ to which the shell material must conform in order to undergo heteroepitaxial growth as a shell. This rationale is strongly supported by the data provided herein, showing that the overgrowth of a thin shell

(1–2 ML) of lattice-mismatched material (e.g. ZnSe) only marginally alters the crystalline lattice of the core material. Instead, the shell material adopts the lattice constant of the core material during initial growth, and substantial deformation of the core only occurs once a shell of substantial thickness is deposited. Therefore, the calculation of the epilayer material quantity can be considered from the perspective of homoepitaxial growth of CdTe on a CdTe substrate, using the bulk density of CdTe and a judiciously chosen monolayer thickness. In this way, the molar quantity of precursors added to grow a specific number of shell monolayers should be the same for all types of materials grown as epitaxial shells, theoretically differing only in the event of defect formation, and the concomitant relaxation of the heterostructure. From this perspective of heteroepitaxy, it is evident that one cannot accurately predict the size of a (core) shell nanocrystal with a predetermined number of monolayers of shell growth unless the strain within both the core and the shell materials are taken into consideration. Initially, the shell material will adopt the lattice constants of the core material, and thus appear larger than expected, if one presumes that the shell material will adopt its bulk lattice constants. This effect will eventually wane as the compressive shell reaches a thickness large enough to compress the core. It should be noted that the 'ideal' calculation method for the deposition of a shell would to be to determine the exact number of unpassivated orbitals on the surface atoms on the QDs, and to add this specific number of elemental precursors to constitute 1.0 ML of shell (or 0.5 ML if the surface facets are polar), and then repeat the process for the next monolayer. However, exact determination of these values is not yet feasible, although theoretically calculated values strongly correlate with the approach used herein.

The volume of shell material comprising *m* monolayers of material can be calculated as:

$$V_{shell}=\frac{4}{3}\pi\left[(r_c+m\times d_{ML})^3-r_c^3\right]$$

where V_{shell} is the volume of shell material per QD, r_c is the radius of the QD core (assuming a spherical geometry), and d_{ML} is the thickness of one monolayer of shell. Here we use d_{ML} = 0.324 nm, the (200) interplanar spacing for zinc blende CdTe. This value was selected based on the preferential growth of the shells on facets parallel to the c-axis. Note that the choice of other interplanar distances, such as the (220) separation distance, could also be justified, although the application of the SILAR growth mechanism is theoretically incompatible with nonpolar facets. The amount of shell material to add can then be calculated using the following formula:

$$n_{shell}=\frac{V_{shell}\times D_{core}\times N_A\times n_{QD}}{MW_{core}}$$

where n_{shell} is the number of moles of each precursor required to deposit *m* ML of shell material, D_{core} is the density of the core material (D_{CdTe} = 5.85 g cm^{-3}), N_A is Avogadro's number, n_{QD} is the number of moles of QDs in solution, and MW_{core} is the molecular weight of the core material. The molar quantities of precursors added for different shell thicknesses on a 3.8 nm core are summarized in Supplementary Table 3, along with their diameters, as determined via TEM, and their expected sizes assuming both a relaxed lattice and a strained, coherent lattice. Note that the cores used for this study were not completely spherical, which impacts the observed sizes of the heterostructures, as described in the main text of this work. The XRD spectra, the observed sizes via TEM, and the preferential orientation of the nanocrystals on TEM grids are all consistent with the preferential growth of the shell in the a-direction of the wurtzite crystal structure, similar to the growth of a cylinder in the radial direction.

Strain and band structure calculations

Band offsets were calculated using a combination of the "model-solid theory" and a continuum elasticity model of concentric spheres, which have been described rigorously in the literature. The method of Balasubramanian et al.[41] was used to calculate the strain and coherency range for a core/shell nanocrystal, which was modeled as a sphere enclosed in a concentric sphere with different lattice parameters and elastic moduli. The critical shell thickness was determined to be that in which the formation of a dislocation loop was more favorable than coherent growth. This was calculated by determining the shell thickness for which the energy of the coherent, elastically strained state is equal to the energy of the incoherent state, with the latter arising from energy from both the defect and the residual elastic energy from strain. With knowledge of the bandgap of the core from optical spectroscopy before capping, the relative energy shifts of the conduction and valence band edges due to quantum confinement were calculated to a first approximation from the relationship

$$\Delta E_{e,h} \propto \frac{1}{m_{e,h}}$$

in which the change in energy of the conduction (valence) band edge due to quantum confinement, $\Delta E_e(\Delta E_h)$, is inversely proportional to the effective mass of the electron (hole).[42] Determination of the band edges of the shell is more difficult, but can be approximated to a surprisingly accurate degree by assuming the shell to behave as a two-dimensional quantum well. This approximation is theoretically acceptable if the perimeter of the sphere is larger than the exciton Bohr diameter of the shell material, such that the radial direction is not quantum confined. The dependence of the bandgap of an unstrained quantum well on its width has been empirically determined and calculated theoretically for many different II-VI materials, and can be found in the literature. Once the bandgaps, band offsets, and material strain of the core and shell materials are known, the model-solid approach of Van de Walle and Martin[43] can be used to approximate the bandgap of the entire heterostructure using published materials parameters for the materials of interest.[25,37,44] There are several advantages and disadvantages to this approach for the determination of band structure. This method is robust and purely analytical, requiring very little computational power to implement. The reliance on empirical data adds credibility, and no correction factor needs to be used for the bandgaps, unlike for local density approximations, although theoretically calculated bandgaps and band offsets could just as easily be used instead. The use of a continuum elastic model of nanocrystals is likely to be less accurate than atomistic elasticity models, especially in regions with abrupt changes in strain, such as in the direct vicinity of nano-heterostructure interfaces, but this approach has been shown to agree strongly with more complex models.[45] However, the model-solid approach does not account for quantum tunneling, which is believed to be an important characteristic of the wave nature of charge carriers for influencing the optical properties of heterostructures, especially for nanocrystals with highly localized charge carriers. It is possible that the accuracy of this model could be increased with the inclusion of a term accounting for the finite well depths of the charge carriers. The nonspherical, anisotropic growth of the nanocrystals described herein, and the anisotropy and possible size-dependence of the materials parameters of these semiconductors, are other sources of error when comparing with this model.

Nanocrystal characterization

Steady-state fluorescence spectra were obtained using a spectrofluorometer from Photon Technology International. A xenon lamp was used for excitation, and the detector was a photomultiplier tube for the spectral range 400–800 nm, and an InGaAs detector was used for the range 800–1700 nm. The spectrometer slit widths were typically operated at 4 nm. Quantum

yield measurements were performed by comparison to Atto dyes (520, 565, 610, or 680) dissolved in ethanol, accounting for differences in solvent refractive index. Absorption spectra were measured on a Shimadzu spectrophotometer with 1 nm slit widths. Time-resolved fluorescence decay spectra were obtained with excitation from a 478 nm pulsed diode laser. A spectrometer was used to resolve the peak emission wavelength, detected using a photomultiplier tube. Transmission electron micrographs were obtained with a Hitachi H-7500 TEM, and high resolution imaging was performed on a Hitachi H-9500. X-ray diffraction spectra were measured using a Bruker SMART 1000 CCD/Hi-Star dual-detector diffractometer, with a cobalt X-ray source.

Supplementary Material

Refer to Web version on PubMed Central for supplementary material.

Acknowledgements

The authors would like to thank Dr. Hong Yi, Dr. Zhong L. Wang, Dr. Yong Ding, and Dr. Amar Kumbhar for assistance with transmission electron microscopy, Dr. Kenneth Hardcastle for help with powder X-ray diffraction, and Dr. Robert Dickson, Dr. Tim Lian, Abey Issac, and Philip Nicovich for help in fluorescence lifetime data measurements. This work was supported by NIH grants (P20 GM072069, R01 CA108468, and U01HL080711, U54CA119338, and PNEY018244), the DOE Genomes to Life (GTL) Program, and the Georgia Cancer Coalition Distinguished Cancer Scholars Program.

References

1. Robinson RD, et al. Spontaneous superlattice formation in nanorods through partial cation exchange. Science 2007;317:355–358. [PubMed: 17641197]
2. Lee J, et al. Bandgap modulation of carbon nanotubes by encapsulated metallofullerenes. Nature 2002;415:1005–1008. [PubMed: 11875563]
3. Suhr J, et al. Fatigue resistance of aligned carbon nanotube arrays under cyclic compression. Nature Nanotech 2007;2:417–421.
4. Hall AR, Falvo MR, Superfine R, Washburn S. Electromechanical response of single-walled carbon nanotubes to torsional strain in a self-contained device. Nature Nanotech 2007;2:413–416.
5. Roberts MM, et al. Elastically relaxed free-standing strained-silicon nanomembranes. Nature Mater 2006;5:388–393. [PubMed: 16604081]
6. Dabbousi BO, et al. (CdSe)ZnS core-shell quantum dots: Synthesis and characterization of a size series of highly luminescent nanocrystallites. J. Phys. Chem. B 1997;101:9463–9475.
7. Manna L, Scher EC, Li LS, Alivisatos AP. Epitaxial growth and photochemical annealing of graded CdS/ZnS shells on colloidal CdSe nanorods. J. Am. Chem. Soc 2002;124:7136–7145. [PubMed: 12059239]
8. McBride J, Treadway J, Feldman LC, Pennycook SJ, Rosenthal SJ. Structural basis for near unity quantum yield core/shell nanostructures. Nano Lett 2006;6:1496–1501. [PubMed: 16834437]
9. Chen XB, Lou YB, Samia AC, Burda C. Coherency strain effects on the optical response of core/shell heteronanostructures. Nano Lett 2003;3:799–803.
10. Maki H, Testuya S, Ishibashi K. Direct observation of the deformation and the band gap change from an individual single-walled carbon nanotube under uniaxial strrain. Nano Lett 2007;7:890–895. [PubMed: 17358091]
11. Li YH, Gong XG, Wei SH. Ab initio all-electron calculation of absolute volume deformation potentials of IV-IV, III-V, and II-VI semiconductors: the chemical trends. Phys. Rev. B 2006;73245206
12. Li JB, Wang LW. Deformation potentials of CdSe quantum dots. Appl. Phys. Lett 2004;85:2929–2931.
13. Brunner K. Si/Ge nanostructures. Rep. Prog. Phys 2002;65:27–72.

14. Lamberti C. The use of synchrotron radiation techniques in the characterization of strained semiconductor heterostructures and thin films. Surf. Sci. Rep 2004;53:1–197.
15. Mueller AH, et al. Multicolor light-emitting diodes based on semiconductor nanocrystals encapsulated in GaN charge injection layers. Nano Lett 2005;5:1039–1044. [PubMed: 15943439]
16. Tan ZN, et al. Bright and color-saturated emission from blue light-emitting diodes based on solution-processed colloidal nanocrystal quantum dots. Nano Lett 2007;7:3803–3807. [PubMed: 17975946]
17. Persson J, Hakanson U, Johansson MKJ, Samuelson L, Pistol ME. Strain effects on individual quantum dots: Dependence of cap layer thickness. Phys. Rev. B 2005;72085302
18. Wei SH, Zunger A. Predicted band-gap pressure coefficients of all diamond and zinc-blende semiconductors: Chemical trends. Phys. Rev. B 1999;60:5404–5411.
19. Peng XG, Schlamp MC, Kadavanich AV, Alivisatos AP. Epitaxial growth of highly luminescent CdSe/CdS core/shell nanocrystals with photostability and electronic accessibility. J. Am. Chem. Soc 1997;119:7019–7029.
20. Kim S, Fisher B, Eisler HJ, Bawendi M. Type-II quantum dots: CdTe/CdSe(core/shell) and CdSe/ZnTe(core/shell) heterostructures. J. Am. Chem. Soc 2003;125:11466–11467. [PubMed: 13129327]
21. Piryatinski A, Ivanov SA, Tretiak S, Klimov VI. Effect of quantum and dielectric confinement on the exciton-exciton interaction energy in type II core/shell semiconductor nanocrystals. Nano Lett 2007;7:108–115. [PubMed: 17212448]
22. Xie R, Zhong X, Basche T. Synthesis characterization, and spectroscopy of type-II core/shell semiconductor nanocrystals with ZnTe cores. Adv. Mater 2005;17:2741–2745.
23. Chen CY, et al. Spectroscopy and femtosecond dynamics of type-II CdSe/ZnTe core-shell semiconductor synthesized via the CdO precursor. J. Phys. Chem. B 2004;108:10687–10691.
24. Jeong S, et al. Effect of the thiol-thiolate equilibrium on the photophysical properties of aqueous CdSe/ZnS nanocrystal quantum dots. J. Am. Chem. Soc 2005;127:10126–10127. [PubMed: 16028897]
25. Adachi, S. Properties of Group-IV, III-V and II-VI Semiconductors. Wes Sussex, England: John Wiley & Sons; 2005.
26. Xie RG, Zhong XH, Basche T. Synthesis, characterization, and spectroscopy of type-II core/shell semiconductor nanocrystals with ZnTe cores. Adv. Mater 2005;17:2741–2745.
27. Wei SH, Zhang SB. Structure stability and carrier localization in CdX (X = S, Se, Te) semiconductors. Phys. Rev. B 2000;62:6944–6947.
28. Talapin DV, et al. Highly emissive colloidal CdSe/CdS heterostructures of mixed dimensionality. Nano Lett 2003;3:1677–1681.
29. Manna L, Wang LW, Cingolani R, Alivisatos AP. First-principles modeling of unpassivated and surfactant-passivated bulk facets of wurtzite CdSe: A model system for studying the anisotropic growth of CdSe nanocrystals. J. Phys. Chem. B 2005;109:6183–6192. [PubMed: 16851684]
30. Goldstein AN, Echer CM, Alivisatos AP. Melting in semiconductor nanocrystals. Science 1992;256:1425–1427. [PubMed: 17791609]
31. Zhang JZ, Zhao YS, Palosz B. Comparative studies of compressibility between nanocrystalline and bulk nickel. Appl. Phys. Lett 2007;90
32. Tolbert SH, Alivisatos AP. High-pressure structural transformations in semiconductor nanocrystals. Annu. Rev. Phys. Chem 1995;46:595–625.
33. Zhang XY, Sharma P, Johnson HT. Quantum confinement induced strain in quantum dots. Phys. Rev. B 2007;75
34. Meulenberg RW, Jennings T, Strouse GF. Compressive and tensile stress in colloidal CdSe semiconductor quantum dots. Phys. Rev. B 2004;70
35. Yeh CY, Lu ZW, Froyen S, Zunger A. Zinc-blende-wurtzite polytypism in semiconductors. Phys. Rev. B 1992;46:10086–10097.
36. Oron D, Kazes M, Banin U. Multiexcitons in type-II colloidal semiconductor quantum dots. Phys. Rev. B 2007;75035330
37. Huynh WU, Dittmer JJ, Alivisatos AP. Hybrid nanorod-polymer solar cells. Science 2002;295:2425–2427. [PubMed: 11923531]

38. Yu WW, Wang YA, Peng XG. Formation and stability of size-, shape-, and structure-controlled CdTe nanocrystals: Ligand effects on monomers and nanocrystals. Chem. Mater 2003;15:4300–4308.

39. Li JJ, et al. Large-scale synthesis of nearly monodisperse CdSe/CdS core/shell nanocrystals using air-stable reagents via successive ion layer adsorption and reaction. J. Am. Chem. Soc 2003;125:12567–12575. [PubMed: 14531702]

40. Jasieniak JJ, Mulvaney P. From Cd-rich to Se-rich-the manipulation of CdSe nanocrystal surface stoichiometry. J. Am. Chem. Soc 2007;129:2841–2848. [PubMed: 17309253]

41. Balasubramanian S, Ceder G, Kolenbrander KD. Three-dimensional epitaxy: Thermodynamic stability range of coherent germanium nanocrystallites in silicon. J. Appl. Phys 1996;79:4132–4136.

42. Efros AL, Efros AL. Interband absorption of light in a semiconductor sphere. Soviet Physics Semiconductors-USSR 1982;16:772–775.

43. Van de Walle CG. Band Lineups and Deformation Potentials in the Model-Solid Theory. Phys. Rev. B 1989;39:1871–1883.

44. Wei SH, Zunger A. Calculated natural band offsets of all II-VI and Ill-V semiconductors: Chemical trends and the role of cation d orbitals. Appl. Phys. Lett 1998;72:2011–2013.

45. He LX, Bester G, Zunger A. Strain-induced interfacial hole localization in self-assembled quantum dots: Compressive InAs/GaAs versus tensile InAs/InSb. Phys. Rev. B 2004;70235316

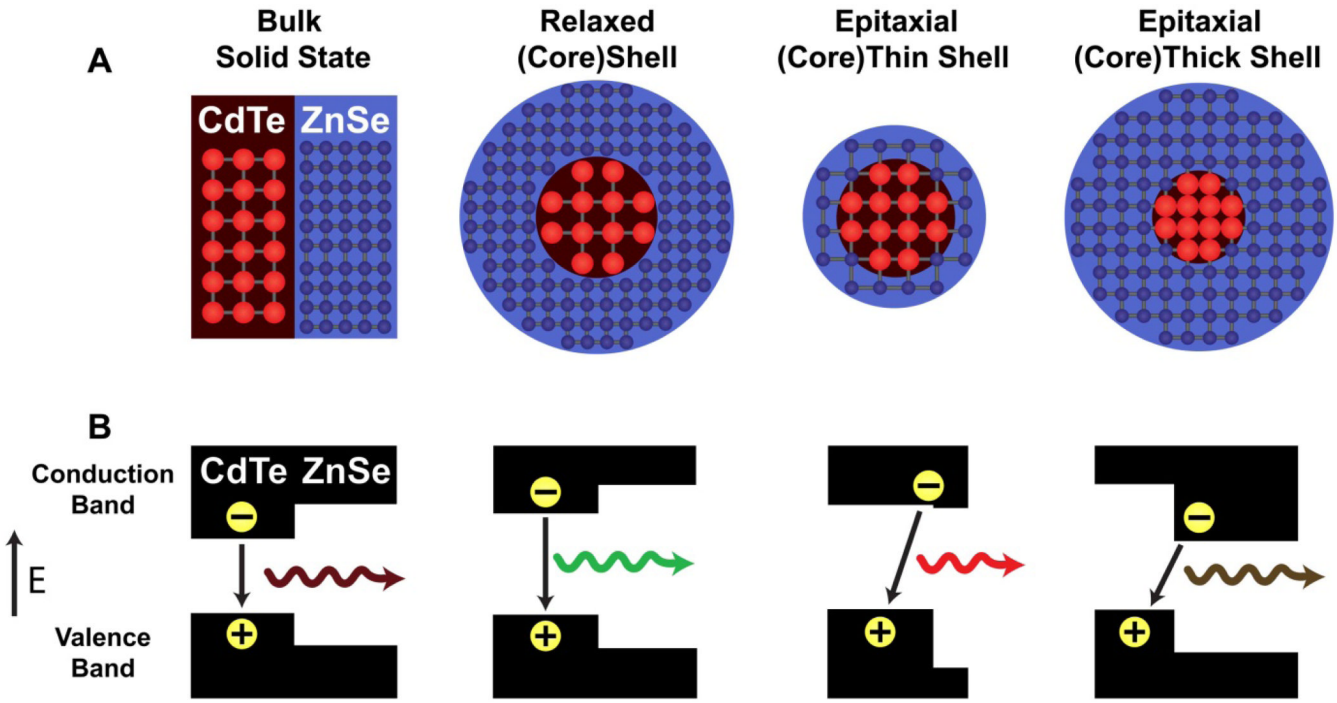

Figure 1. Schematic illustration of band energy changes in semiconductor quantum dots induced by lattice strain

(**A**) Lattice structures of ordinary and strained (CdTe)ZnSe heterojunctions. From left to right: bulk (CdTe)ZnSe marterial, a relaxed (CdTe)ZnSe dot, a strained CdTe core with a markedly "stretched" ZnSe shell (thin), and a markedly "squeezed" CdTe core with a strained ZnSe shell (thick). (**B**) Valence and conduction band energy levels corresponding to bulk, relaxed, and strained (CdTe)ZnSe heterostructures in (**A**). Note that relaxed (CdTe)ZnSe nanostructures are standard type-I QDs, but are converted into type-II behavior when both the core and shell are strained by epitaxial growth. The electrons and holes are colocalized in type-I QDs, whereas they are spatially separated into the shell and the core in type-II QDs (see text for discussion). Discrete electronic energy levels caused by quantum confinement are omitted for simplicity. The impact of strain on band structures is calculated by using the model-solid theory and a continuum elasticity model (see **Methods**).

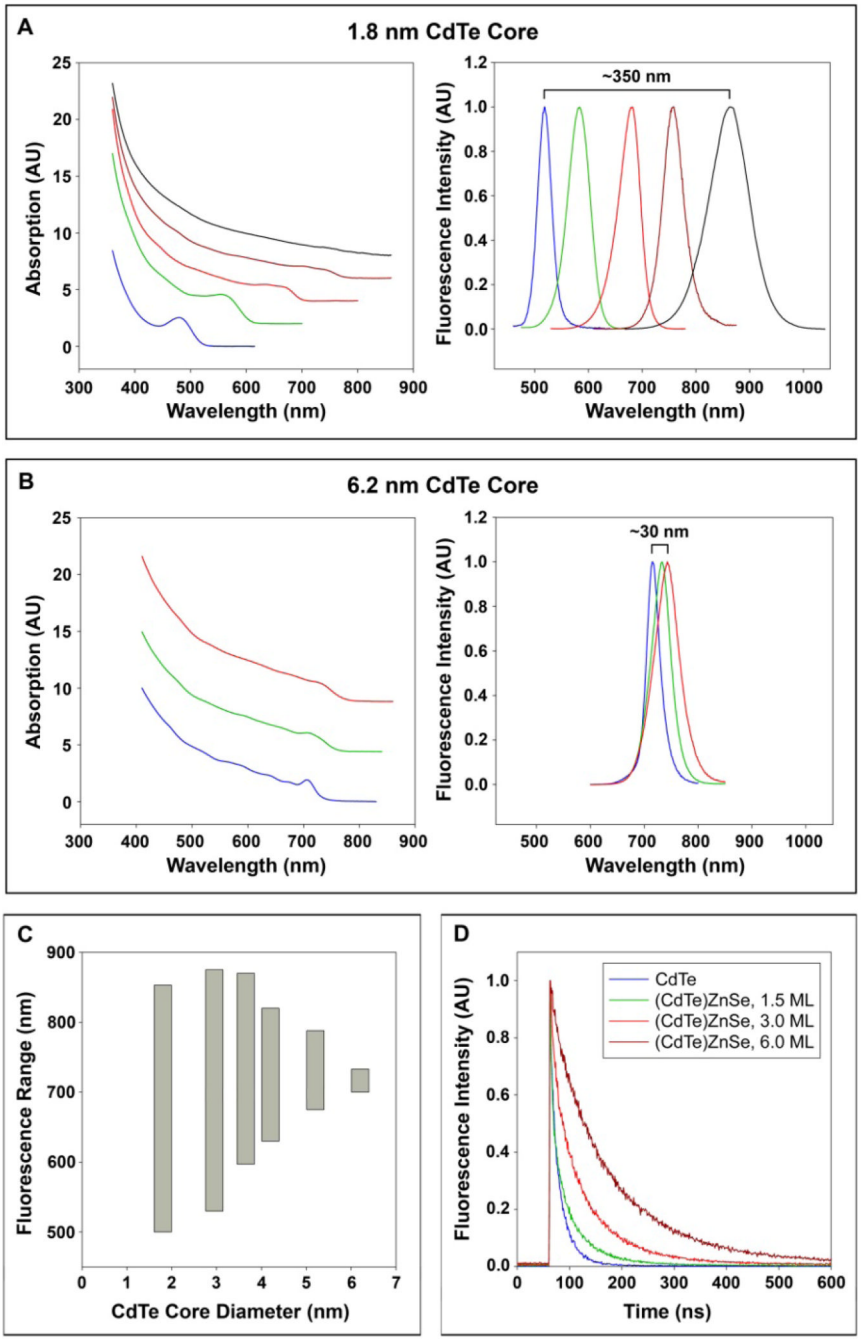

Figure 2. Optical properties of strain-tuned QDs with different CdTe core sizes (1.8 – 6.2 nm) and shell thicknesses (0 – 5 ZnSe monolayers)

(**A**) Absorption (left) and fluorescence emission (right) spectra of (CdTe)ZnSe QDs with 1.8 nm CdTe cores (blue), and capped with 0.5 (green), 1.0 (red), 3.0 (brown), or 6.0 (black) monolayers of ZnSe shell. The thickness of one monolayer of ZnSe is 2.83 angstroms. (**B**) Absorption (left) and fluorescence emission (right) spectra of (CdTe)ZnSe QDs with 6.2 nm CdTe cores (blue), and capped with 2.0 (green) and 5.0 (red) monolayers of ZnSe shell. (**C**) Strain-tunable spectral ranges for different CdTe core sizes, as measured by the fluorescence emission peaks with 0–5 monolayers of shell growth. Epitaxial growth on cores larger than 6.2 nm was not successful. (**D**) Time-resolved fluorescence decay curves of 3.8 nm CdTe QDs

with 0 (blue), 1.5 (green), 3.0 (red), or 6.0 (brown) monolayers of ZnSe shell. The excited state lifetimes were calculated to be 18.4, 35.5, 59.8, and 115.0 ns, respectively. A pulsed 478 nm diode laser was used for excitation.

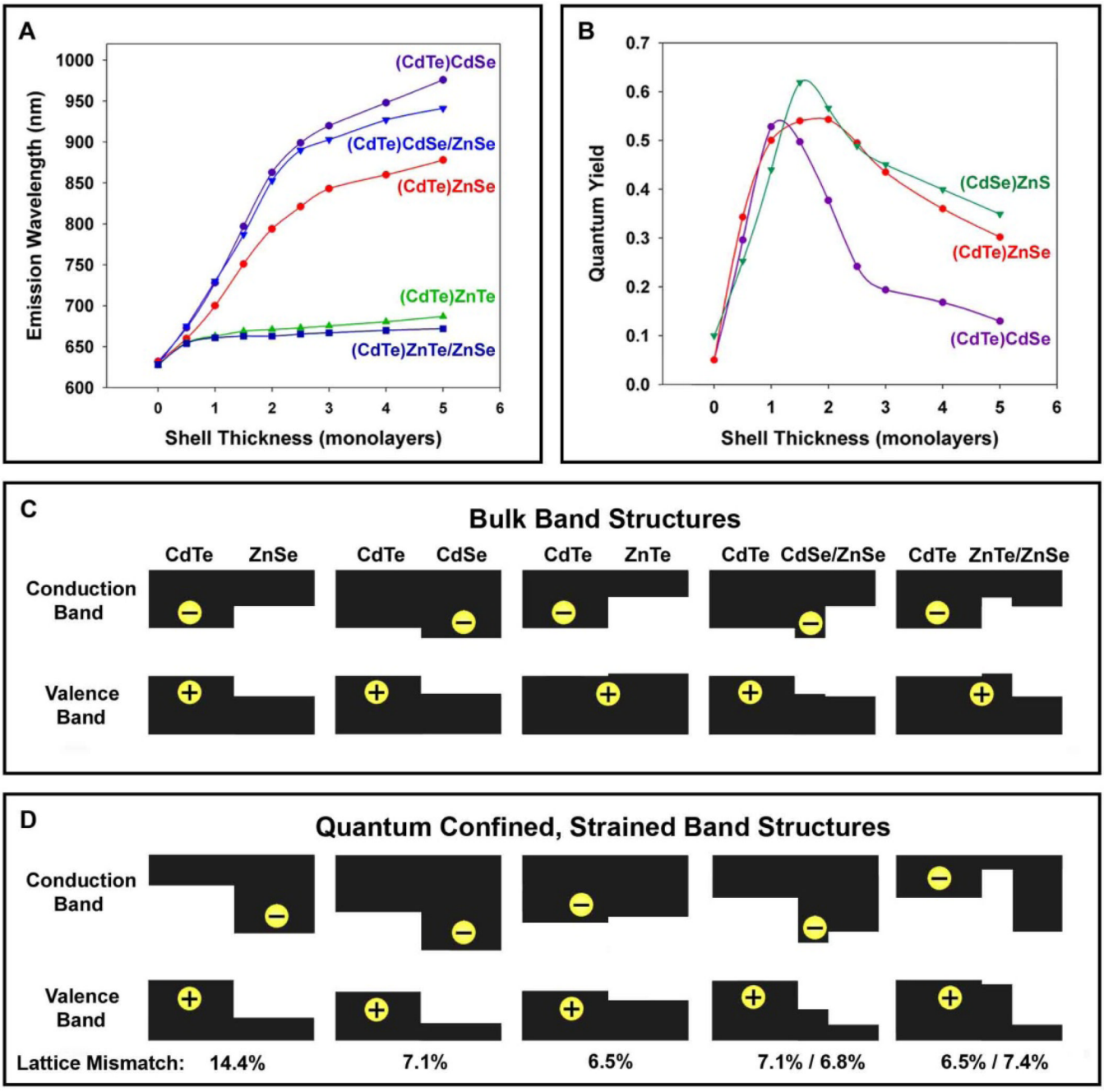

Figure 3. Comparison of emission wavelengths and fluorescence quantum yields for CdTe cores coated with different shell materials and thicknesses

(**A**) Emission wavelengths of 3.8 nm CdTe cores capped with ZnSe, CdSe, or ZnTe, or one monolayer of ZnTe followed by ZnSe (ZnTe/ZnSe), or one monolayer of CdSe followed by ZnSe (CdSe/ZnSe). (**B**) Fluorescence quantum yields of 3.8 nm CdTe cores capped with either ZnSe or CdSe, and CdSe QDs (3.8 nm) capped with ZnS for different shell thicknesses. (**C**) Diagrams of band offsets for core/shell nanocrystals in (**A**), as calculated by using the model-solid theory and a continuum elasticity model for the impact of strain (see **Methods**).

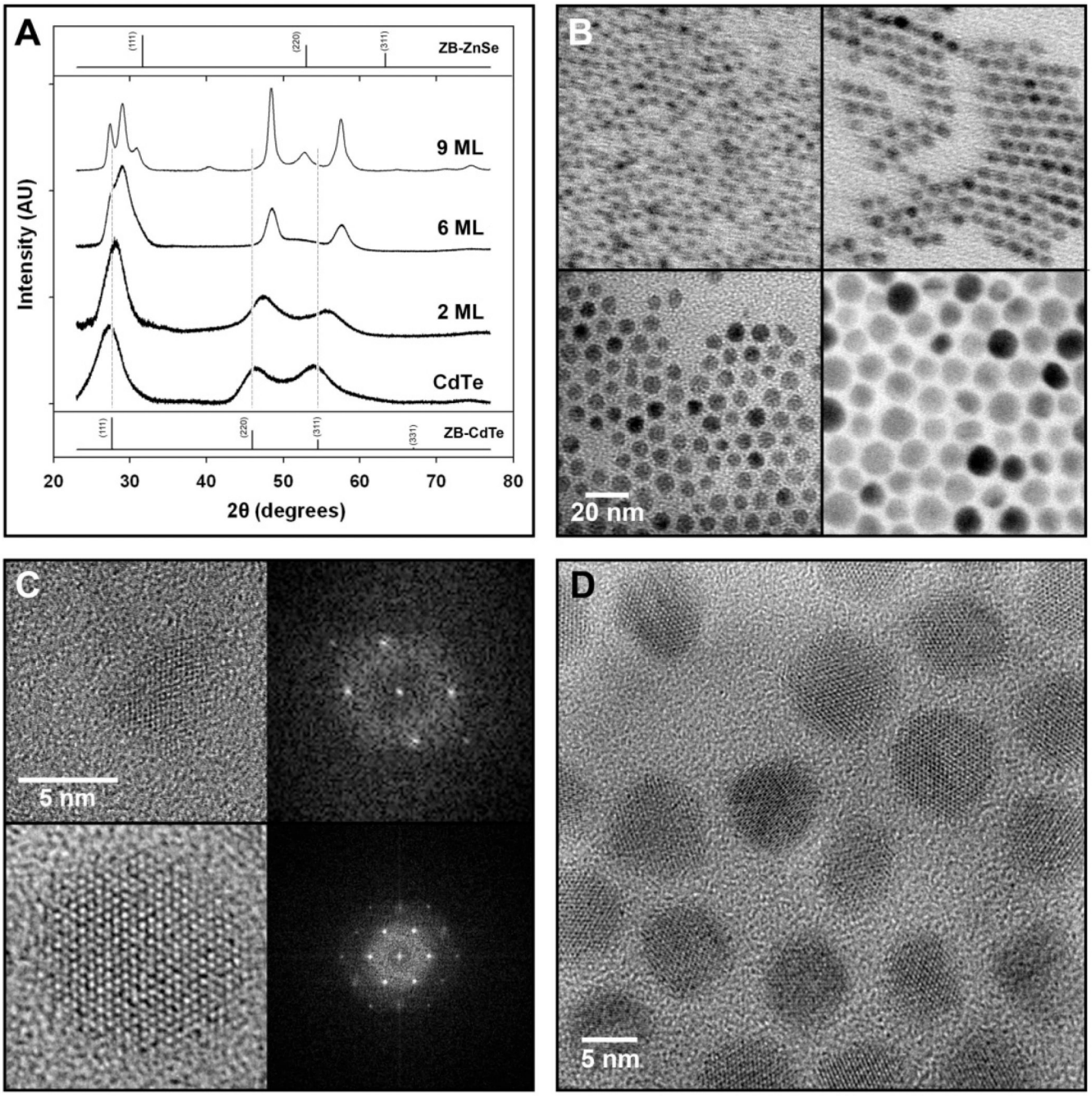

Figure 4. Lattice structures of strain-tunable QDs as determined by power x-ray diffraction and high-resolution transmission electron microscopy

(**A**) Powder x-ray diffraction patterns for 3.8 nm CdTe QDs, and (CdTe)ZnSe QDs with 2, 6, or 9 monolayers of shell growth, from bottom to top. Bulk diffraction peaks for zinc blende (ZB) CdTe and ZnSe are indexed at the bottom and top, respectively, and vertical lines correspond to the major diffraction lines of CdTe. The x-ray wavelength was 1.78897 Å. (**B**) Transmission electron micrographs of 3.8 nm CdTe cores capped with 0 (top left), 2 (top right), 6 (bottom left), and 9 (bottom right) monolayers of ZnSe. (**C**) High-resolution transmission electron micrographs of 3.8 nm CdTe QDs (top) and (CdTe)ZnSe QDs with 6 monolayers of shell (bottom). Fast-Fourier transform spectra of these materials are shown on the right. (**D**)

HRTEM of (CdTe)ZnSe QDs with 6 monolayers of shell, showing all QDs to be oriented with the (001) lattice plane parallel to the substrate. *The absorption and emission spectra of these (core)shell QDS are provided in Supplementary Figure 4, and their simulated diffraction and particle size distribution data are shown in Supplementary Figures 4 and 5. The results obtained from a line-wdith analysis of the diffraction peaks are summarized in Supplementary Table 1.*

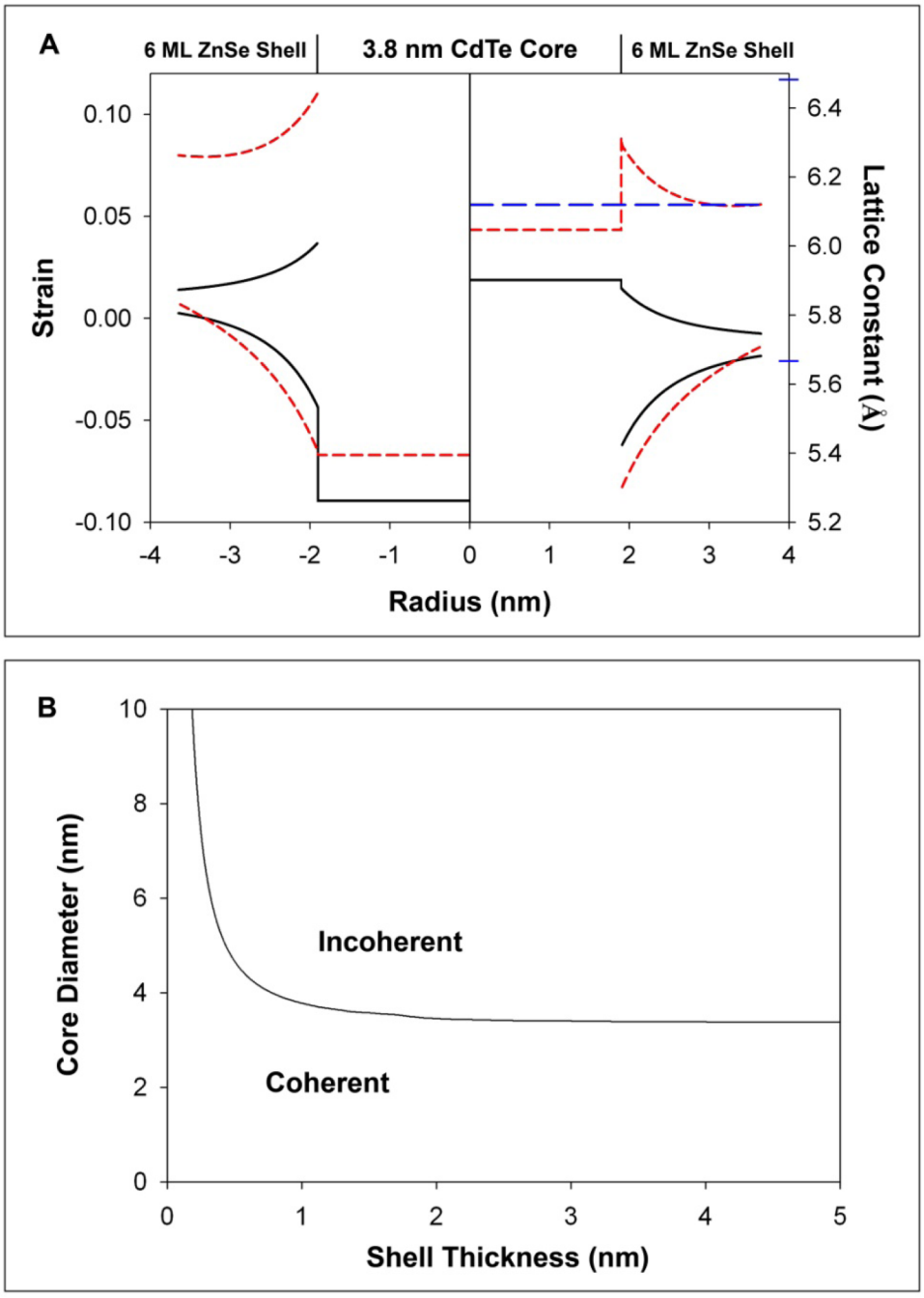

Figure 5. Theoretical predictions of high strain (CdTe)ZnSe QDs from a continuum elasticity model

(**A**) Left axis: strain distribution in 3.8 nm-diameter CdTe nanocrystals capped with 6 monolayers of ZnSe shell. The solid black line indicates strain for the QDs modeled as concentric spheres, and the red hatched lines as concentric cylinders. Strain within the core is compressive and isotropic, while the strain in the shell is compressive in the radial direction (bottom line) and tensile in the tangential direction (top line). Right axis: Calculated lattice constants corresponding to strain profiles for strained, concentric, core/shell spheres and cylinders. The blue hatched line shows the observed lattice constant, determined from XRD and TEM. Blue indices on the axis depict the bulk lattice constants of CdTe (6.482 Å) and ZnSe (5.6676 Å). (**B**) The critical thickness (black line) is the shell thickness for which the

formation of a dislocation loop is energetically more favorable than coherent, epitaxial growth for different core sizes and shell thicknesses.